Modification of Specific Barrier Model Using New Time Functions for Inclined Fault

Naser Khaji[1*] and Mohammad Hadi Rezaei[2]

1. Professor of Civil and Environmental Engineering, Tarbiat Modares University, Tehran, Iran,
* Corresponding Author; email: nkhaji@modares.ac.ir
2. Ph.D. of Earthquake Engineering, Tarbiat Modares University, Tehran, Iran

Received: 04/09/2017
Accepted: 18/02/2018

ABSTRACT

In the specific barrier model (SBM) as an earthquake source model, fault is assumed as a rectangle whose surface is covered by an aggregate of circular cracks of equal diameter (primary version) on which a local stress drop takes place to simulate high-frequency movements. Seismic moment in the SBM is computed in a deterministic manner on the fault plane, on the basis of moment and area constraints. In the SBM, rupture on cracks causes a stress drop that moves within circular cracks, and rupture tip sweeps the fault plane. In this paper, new time functions for inclined faults have been developed. The mentioned time functions have been obtained by using probability density functions (PDFs) of arrival time based on site positions, fault geometry and fault rotation angle. Finally, to calculate source spectra, PDFs of sub-events' size are assumed to be fractal. Various parameter studies are then conducted to show different features of the proposed PDFs on the results of the SBM.

Keywords:
Strong ground motion; Specific barrier model; Inclined fault; Far-field source spectra; Probability density functions

1. Introduction

Earthquakes are one of the most dramatic hazards that are likely to cause heavy human losses and to destroy an entire city on scale of minutes. The more recent damaging events in Kobe (1995 Japan) in Chi Chi (1999 Taiwan) or Bam (2003 Iran) recall that little is known about earthquake physics so far that could prevent people from their deadly effects. To reduce casualties, decades of research involving numerous laboratories worldwide aim at investigating this large-scale phenomenon and trying to understand how it triggers, initiates, propagates, and stops. A trusty physical modeling of strong ground motion requires to examine three crucial parameters of seismic source specifications, wave propagation path, and seismic site effects. Among various seismic source specifications, a more physically realistic source model is the specific barrier model (SBM) proposed and implemented by Papageorgiou and Aki [1-2] based on ω-square model, which developed by Aki [3] and modified by Brune [4]. The SBM is specifically more suitable for regions with poor seismological data bank and/or ground motions from large earthquakes with large recurrence intervals.

In order to simulate seismic ground motions from a specific earthquake source model in an efficient way, the stochastic modeling method has been widely used (see [5]). An essential part of the seismological model used in this method is the quantitative description of the far-field spectrum of seismic waves emitted from the seismic source. Since shear (S) wave is primarily the main factor of earthquake damages, the application of stochastic approach of the SBM has almost been focused on the far-field S wave spectrum, in which two corner frequencies of observed earthquake are represented.

The 'two-corner-frequency' shows two considerable length-scales of an earthquake source: a length-scale that quantifies the overall size of the fault that ruptures (e.g., the length L of a strike-slip fault) and another length-scale that measures the size of the subevents. Associated with these length-scales are two corresponding time scales: (1) the overall duration of rupture, and (2) the rise time. The SBM has a few main source parameters calibrated to earthquakes of different tectonic regions (see for example, Halldorsson and Papageorgiou [6], Zafarani et al. [7], Soghrat et al. [8] and Mousavi et al. [9] among others).

The SBM may be considered as a general idealization of the faulting process of an earthquake [10]. For example, a uniform probability density function (PDF) of 'arrival times' is assumed in the SBM. In this paper, the effects of fault rotation on PDFs of arrival times as well as on the far-field source spectrum of the SBM are studied. For this purpose, direct simulations of ground motion records for an earthquake source, which have fractally-distributed subevent sizes, is used [11-14]. In this research, a new non-uniform more realistic PDF of arrival times for seismic waves corresponding to the fault's geometry and rotation is derived to rich desirable time functions. Afterwards, by using the proposed time functions, the effect of site position to the fault on source spectra, as well as the effect of rotation angle of the fault on time functions, are investigated.

2. The Specific Barrier Model

The SBM provides a quantitative description of heterogeneous rupture. As the main assumption of the SBM, the seismic source is illustrated by a rectangular fault of length L and width W filled by circular subevents of equal diameter, $2\rho_o$, as shown in Figure (1). The SBM represents a physical source model that, in a self-consistent way, describes the earthquake processes with high-frequency seismic ground motion [10], which have two corner-frequencies [15-16]. In the SBM, the earthquake is assumed as a sum of circular ruptures as subevents taking place independently. Furthermore, the rupture front sweeps the fault plane with constant rupture velocity, V, while a stress drop of $\Delta\sigma_L$ occurs in the circular cracks to present each subevent ruptures. The cracks start from the center of the circle and radially spread with a constant spreading velocity, v, until their stopping at the barriers. Halldorsson [6], added high-frequency source complexity factor, ζ, to the previous experssion of source acceleration spectrum of the SBM to modify the model. Consequently, the SBM acceleration spectrum may be given by:

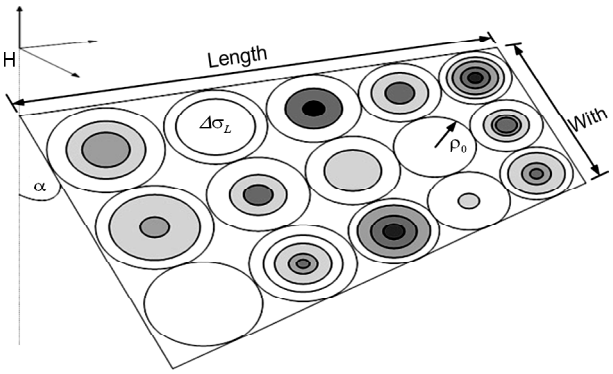

Figure 1. Schematic view of the SBM, which considers an earthquake as random occurrence of some circular cracks. The fault is a plane including some circular cracks, in which local stress drops occur. The equal-size subevents are arranged in a non-overlapping pattern on the fault plane.

$$S(M_0,f,\zeta)= \sqrt{N\zeta+N(N-\zeta)\left(\frac{\sin\pi fT_0}{\pi fT_0}\right)^2}\,(2\pi f)^2\widetilde{M}_{oi}(f) \quad (1)$$

where N denotes the number of subevents, T_0 is the duration of pulsetrain (emitted by the subevents as they rupture) that is received at the station, $\widetilde{M}_{oi}(f)$ indicates the source displacement spectrum of a single sub-event, and ζ scales with magnitude of earthquake as:

$$\zeta=10^{2\eta} \quad , \quad \eta=s_m(M_w-M_{cr}) \quad (2)$$

in which s_m = -0.12, and M_{cr} = 6.35. In the SBM, the source spectra is computed for ζ= 1. As the earthquake events are considered as a composition of subevents, the source spectrum is an aggregate spectrum of all sub-events as:

$$S(\omega)=\sum_{j=1}^{N} S_j(\omega,R_j)\,e^{-i\omega T_j} \quad (3)$$

where T_j implies the time that seismic energy radiated by subevent j arrives ($0<T_j<T_0$), and S_j is the sub-event spectrum expressed by:

$$S_j = \frac{M_{oi}}{1+\left(f/f_2\right)^2} \tag{4}$$

in which M_{oi} is the seismic moment of sub-event *i*, and f_2 denotes the corner frequency. In addition, the seismic moment is given by:

$$M_{oi} = \frac{16}{7}\Delta\sigma_L R^3 \tag{5}$$

where $\Delta\sigma_L$ is local stress drop, and *R* indicates the random radius of circular cracks. Besides, corner frequency is given by:

$$f_2 = \frac{c_s \beta}{2\pi R} \tag{6}$$

where β is the *S* wave velocity, c_s indicates an increasing function of v/β. According to the results of Papageorgiou [10], $1.72 \le c_s \le 1.85$ for $0.7 \le v/\beta \le 0.9$.

The expected value of source spectrum may be given by:

$$E\left[S(\omega)\right] = E\left[\sum_{j=1}^{N} S_j(\omega, R_j)\, e^{-i\omega T_j}\right] \tag{7}$$

In addition, the expected value of the squared modulus of the aggregate spectrum of radiated seismic energy from the composite earthquake source is illustrated by the following expression; [13]:

$$\begin{aligned} &E\left[\left|S(\omega)\right|^2\right] = \\ &E\left[\left(\sum_{j=1}^{N} S_j(\omega, R_j)\, e^{-i\omega T_j}\right)\left(\sum_{k=1}^{N} S_k^*(\omega, R_k)\, e^{i\omega T_k}\right)\right] = \\ &\sum_{j=1}^{N}\sum_{k=1}^{N} E\left[S_j(\omega, R_j) S_k^*(\omega, R_k)\, e^{-i\omega T_j} e^{i\omega T_k}\right] \end{aligned} \tag{8}$$

in which $(\cdot)^*$ indicates the complex conjugate. If one assumes that the variables are independent, Equation (8) may be rewritten as:

$$\begin{aligned} &\left[\left|S(\omega)\right|^2\right] = \\ &\sum_{j=1}^{N} E\left[\left|S(\omega, R_j)\right|^2\right] + \sum_{j=1}^{N}\sum_{k=1,\,k\neq j}^{N} E\left[e^{-i\omega T_j}\right] \times \\ &E\left[e^{i\omega T_k}\right] E\left[S_j(\omega, R_j) S_k^*(\omega, R_k)\right] \end{aligned} \tag{9}$$

where

$$E\left[e^{-i\omega T_j}\right] = \int_{-\infty}^{\infty} f_{T_i}(t_j)\, e^{-i\omega t_j}\, dt_j \tag{10}$$

in which T_j denotes the arrival time of seismic energy, and $f_{T_i}(t_j)$ is the PDF of arrival time. If one assumes that the PDFs of arrival time are the same for all cracks, and also all R_j follow the same probability distribution, Equation (9) may be rewritten as follows:

$$\begin{aligned} &E\left[\left|S(\omega)\right|^2\right] = \\ &N \cdot E\left[\left|S_R(\omega, R)\right|^2\right] + N(N-1) \times \\ &\left(\left|\int_{-\infty}^{\infty} f_{T_i}(t_j)\, e^{-i\omega t_j}\, dt_j\right|\right)^2 \cdot \left\{E\left[S_R(\omega, R)\right]\right\}^2 \end{aligned} \tag{11}$$

where $\left(\left|\int_{-\infty}^{\infty} f_{T_i}(t_j)\, e^{-i\omega t_j}\, dt_j\right|\right)^2$ is called the time function of the source spectrum. Obviously, the square root of Equation (9) provides the Fourier amplitude of the source spectrum. In order to compute $E\left[\left|S(\omega)\right|^2\right]$ of Equation (11), $f_R(\mathrm{r})$ and $f_T(\mathrm{t})$ are required. For $f_R(\mathrm{r})$, the PDF with fractal distribution [13] is used in this paper (see the next section). However, $f_T(\mathrm{t})$ is derived based on a new approach in this research, as discussed in the following sections.

3. The PDFS of Subevent Sizes

The PDFs of subevent sizes used in this research are exact PDFs, which have been developed by Halldorsson [13]. The main purpose of this section is therefore a brief review of their presented PDFs for size of circular cracks. By introducing parameters α_1 and α_2, they relaxed the equal-size limitation regarding subevents of the SBM. In other words, they allowed the circles' radius to vary between R_a and R_b as given by

$$R_b = \alpha_1 R_c \tag{12}$$

$$R_a = \alpha_2 R_b = \alpha_1 \alpha_2 R_c \tag{13}$$

where R_c denotes the radius of circular fault which has the same area as the main fault.

By assuming that total seismic moment of subevents that compose the composite source are equal to the seismic moment M_0^c of the main event, one may write:

$$M_0^c = \int_{R_a}^{R_b} M_{o_1}(r)\, n_R(r)\, dr \tag{14}$$

in which $n_R(r)$ denotes a frequency-size 'density' function, and $n_R(r)\,dr$ determines the number of subevents with radii $r < R < r + dr$ [12]. They assumed a composite source including subevents, the size distribution of which may be given by:

$$\frac{dN_R(r)}{d\ln r} = pr^{-D} \tag{15}$$

in which D denotes the fractal dimension ($D = 2$ or 3, according to Frankel, [11]), $n_R(r)$ indicates the number of subevents with radius larger than a given value r, and p is a constant of proportionality, which is determined by the moment constraint. Integrating Equation (15) results in the following expression:

$$N_R(r) = \frac{p}{D}\left(r^{-D} - R_b^{-D}\right) \tag{16}$$

in which $N_R(r)$ denotes the number of subevents with radius larger than r. In addition, $N_R(r)$ may be considered as a frequency-size 'complementary distribution' function, which is related to the function $n_R(r)$ as:

$$n_R(r) = -\frac{dN_R(r)}{dr} \tag{17}$$

Besides, it may be shown that:

$$F_R(r) = \frac{N - N_R(r)}{N} \tag{18}$$

and

$$f_R(r) = \frac{1}{N} n_R(r) \tag{19}$$

By assuming D, one may have the PDF of subevent sizes. Such a model has been implemented for ground motion simulations by Zeng [12], where the PDF of sub-event sizes is:

$$f_R(r) = \frac{D\,R_a^D R_b^D}{R_b^D - R_a^D}\frac{1}{r^{D+1}} \tag{20}$$

By using the obtained PDF, one may compute the following parameters of the source spectrum of a composite source [13]. For $D = 2$,

$$\left\{E\left[\left|S_R(\omega,R)\right|\right]\right\}^2 = \left(\frac{16\Delta\sigma_L}{7}\cdot\frac{c_s\beta}{\omega}\cdot\frac{2R_a^2R_b^2}{R_b^2-R_a^2}\right)^2 \times \left(\tan^{-1}\left(\frac{\omega R_b}{c_s\beta}\right) - \tan^{-1}\left(\frac{\omega R_a}{c_s\beta}\right)\right)^2 \tag{21}$$

$$E\left[\left|S_R(\omega,R)\right|^2\right] = \left(\frac{16\Delta\sigma_L}{7}\cdot\frac{c_s\beta}{\omega}\right)^2\cdot\frac{R_a^2R_b^2}{R_b^2-R_a^2}\cdot \left[\frac{R_a^2-R_b^2}{\left(1+\left(\frac{\omega R_b}{c_s\beta}\right)^2\right)\left(1+\left(\frac{\omega R_a}{c_s\beta}\right)^2\right)} + \frac{(c_s\beta)^2}{\omega^2}\ln\frac{\left(1+\left(\frac{\omega R_b}{c_s\beta}\right)^2\right)}{\left(1+\left(\frac{\omega R_a}{c_s\beta}\right)^2\right)}\right] \tag{22}$$

and

$$N = \frac{1}{16}\left(\alpha_2^2+4\alpha_2+1\right)\frac{(1-\alpha_2)^2}{\alpha_2^2} + \sqrt{\left(\alpha_2^2+4\alpha_2+1\right)^2\frac{(1-\alpha_2)^4}{256\alpha_2^4} + \left(\frac{1+\alpha_2}{2\alpha_1^3\alpha_2^2}\right)^2\left(\frac{\Delta\sigma_G}{\Delta\sigma_L}\right)^2} \tag{23}$$

and for $D = 3$,

$$\left\{E\left[\left|S_R(\omega,R)\right|\right]\right\}^2 = \left(\frac{16\Delta\sigma_L}{7}\right)^2\left(\frac{3R_a^3R_b^3}{R_b^3-R_a^3}\right)^2\times \left(\ln\frac{R_b\sqrt{\left(1+\left(\frac{\omega R_a}{c_s\beta}\right)^2\right)}}{R_a\sqrt{\left(1+\left(\frac{\omega R_b}{c_s\beta}\right)^2\right)}}\right)^2 \tag{24}$$

$$E\left[\left|S_R(\omega,R)\right|^2\right] = \left(\frac{16\Delta\sigma_L}{7}\cdot\frac{c_s\beta}{\omega}\right)^2\times \left[-\left(\frac{R_b}{1+\left(\frac{\omega R_b}{c_s\beta}\right)^2}-\frac{R_a}{1+\left(\frac{\omega R_a}{c_s\beta}\right)^2}\right)+\left(\frac{c_s\beta}{\omega}\right)\times \left(\tan^{-1}\left(\frac{\omega R_b}{c_s\beta}\right)-\tan^{-1}\left(\frac{\omega R_a}{c_s\beta}\right)\right)\right]\frac{3R_a^3R_b^3}{2\left(R_b^3-R_a^3\right)} \tag{25}$$

and

$$N=\frac{\left(9\ln^2\alpha_2+2\right)\alpha_2^3-\alpha_2^6-1}{18\alpha_2^3\ln^2\alpha_2}+\sqrt{\left(\frac{\left(9\ln^2\alpha_2+2\right)\alpha_2^3-\alpha_2^6-1}{18\alpha_2^3\ln^2\alpha_2}\right)^2+\left(\frac{\left(1-\alpha_2\right)\left(\alpha_2^2+\alpha_2+1\right)}{3\alpha_2^3\alpha_1^3\ln^2\alpha_2}\right)^2\left(\frac{\Delta\sigma_G}{\Delta\sigma_L}\right)^2} \quad (26)$$

In this study, the subevents have the PDFs for which the fractal dimension (D) is equal to 2 and 3. Results of this section is combined with the proposed new time function of the next section, to provide earthquake source spectra of the SBM (for more details, refer to the main reference [13]).

4. The PDF of Arrival Time

In primary version of the SBM, the PDF of arrival time was assumed to be uniform. In other words, all points on the fault have the same chance to reach to receiver positions, in the specific period of 0 to T_0. Based on this assumption, the PDF of arrival time of seismic waves may be given by:

$$f_T(t)=\frac{1}{T_0}\quad,\quad t\in[0,\ T_0] \quad (27)$$

The squared amplitude of the Fourier transform of $f_T(t)$ is written as:

$$\left(\left|\bar{f}_T(\omega)\right|\right)^2=\left(\sin\frac{\omega T_0}{2}\right)^2/\left(\frac{\omega T_0}{2}\right)^2 \quad (28)$$

However, in real situation, for the points closer to the receiver position, the seismic energy has a better chance to get to the receiver position, faster. Accordingly, Halldorsson and Papageorgiou [14] extracted the PDF of arrival time by expanding circular rupture tip originating at the supposed hypocenter. In their method, a specific point should be assumed to be the hypocenter from which the whole rupture begins. By choosing different hypocenters, various PDFs are then obtained.

The purpose of the present study is to develop a more general approach that considers the geometry of fault and site positions as well as the position of hypocenter to consider the effect of both factors, the arrival time of seismic waves divided to two parts. The first part regarding to geometry of fault and site position, and the second part regarding to the rupture direction (position of hypocenter). In this method, the appropriate PDF of arrival time is simply computed by making various zones on the fault, based on their distance from a given receiver on the ground surface and from the hypocenter.

To find the first part of the arrival time of seismic waves, regardless of the position of hypocenter, fault must divide to portions with the different distance from receiver. In fact, seismic waves are most likely to be sooner received by a specific receiver, from the points of fault with less distance, compared to the farther points. Consequently, the probability of arrival of seismic waves (regardless of position of hypocenter) in certain time window may be easily obtained. To this end, a large number of points on the ground surface are chosen as receiver positions for which the PDFs of arrival time are obtained.

Figure (2) shows the position of the considered typical fault, as well as the location of assumed receivers on the ground. In order to calculate the PDF of arrival time for any receiver position, it is necessary to specify the areas with the same distance from the receiver on the fault. For this purpose, several spheres of various radius are drawn, whose centers are located on the given receivers. Figure (3) illustrates the intersection of the fault and a typical sphere. Therefore, a group of different curves are produced by the intersection of different spheres and the fault plane (see Figure 4). All points in the region between the semi-parallel adjacent curves are considered to have the same distance from the receiver (the center of various spheres). This means that all points surrounded by two adjacent curves have equal chance to get to the receiver position. Consequently, for creating the PDF of arrival time of seismic waves, the chance of arriving

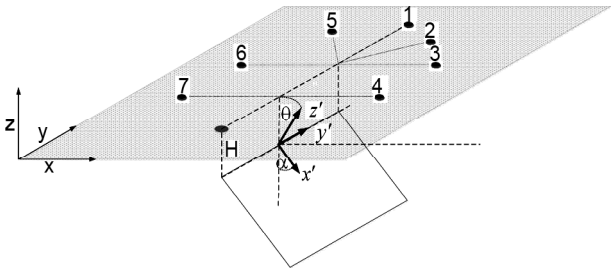

Figure 2. Position fault underground, new coordinate system and selected stations.

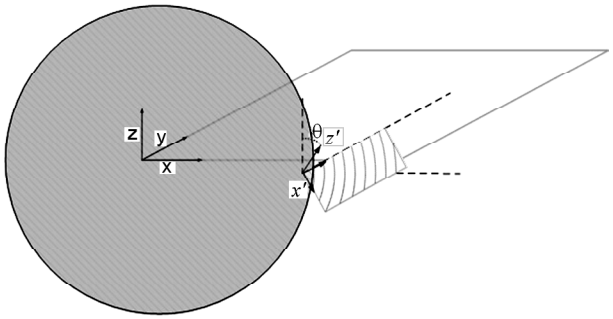

Figure 3. To divide the fault surface according to the distance from the station position, a typical sphere is drawn, whose intersection with the fault plane is appeared in a typical curve, which represents the points with the identical distance from the station.

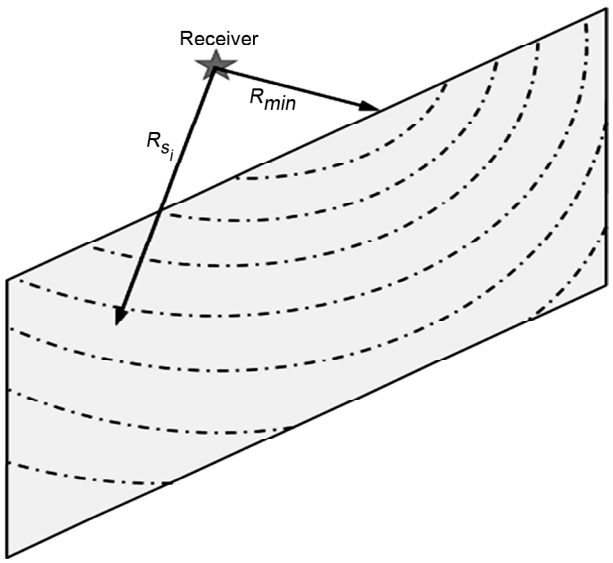

Figure 4. These curves are results of intersecting the fault plane and spheres with different radiuses, and divide the fault points based on their distance from the receiver location.

seismic wave in specific time window should be determined, based on the above-mentioned simple assumption. By changing distance parameter to time parameter, the PDF of arrival time of seismic waves may be easily obtained.

In order to find mentioned areas on the fault, a rectangular fault with dimensions of $L \times W$ located in H depth, is considered. Mentioned fault can rotate around y' axis. Assuming x' y' z' coordinates system as shown in Figure (2), the fault plane may be given by the following equation:

$$z' = 0 \ , \quad -\frac{L}{2} < x' < \frac{L}{2} \ , \quad H < y' < H + W \tag{29}$$

The equation of the sphere shown in Figure (4) may be written as:

$$(x-a)^2 + (y-b)^2 + (z-c)^2 = r_i^{\,2} \tag{30}$$

If (i, j, k) is unite vector in main coordinate system and (i', j', k') is unite vector in new coordinate system, position of each point in main coordinate system can be recognized in new one by multiplying rotate matrix (R) in main system ($p_{(x'y'z')} = R p_{(xyz)}$) in which $p_{(xyz)}$ is coordinate of a point in main system, $p_{(x'y'z')}$ is coordinate of the same point in new system. As mentioned before, R is the rotate matrix defined as:

$$\begin{bmatrix} p_{x'} \\ p_{y'} \\ p_{z'} \end{bmatrix} = \begin{bmatrix} i_{x'}.i_x & i_{x'}.j_y & i_{x'}.k_z \\ j_{y'}.i_x & j_{y'}.j_y & j_{y'}.k_z \\ k_{z'}.i_x & k_{z'}.j_y & k_{z'}.k_z \end{bmatrix} . \begin{bmatrix} p_x \\ p_y \\ p_z \end{bmatrix} \tag{31}$$

If rotation is assumed to be around y and the amount of rotation considered to be θ, the rotate matrix would be:

$$R = \begin{bmatrix} \cos\theta & 0 & \sin\theta \\ 0 & 1 & 0 \\ -\sin\theta & 0 & \cos\theta \end{bmatrix} \tag{32}$$

Therefore, the coordinate of points in new system would be:

$$\begin{bmatrix} a' \\ b' \\ c' \end{bmatrix} = \begin{bmatrix} \cos\theta & 0 & \sin\theta \\ 0 & 1 & 0 \\ -\sin\theta & 0 & \cos\theta \end{bmatrix} . \begin{bmatrix} a \\ b \\ c \end{bmatrix} \tag{33}$$

Thus, one can rewrite Equation (30) as:

$$(x'-a')^2 + (y'-b')^2 + (z'-c')^2 = r_i^{\,2} \tag{34}$$

where (a', b', c') denotes the coordinates of the receiver in new coordinate system, and r_i is the radius of (i)th typical sphere. The intersection curves of the fault plane and the (i)th typical spheres, as schematically depicted in Figure (4), may be derived as:

$$(x'-a')^2 + (y'-b')^2 = r_i^{\,2} - c'^2 \tag{35}$$

Equation (35) shows that the intersection between fault plane and assumed sphere is a circle the center of which may be written as:

$$x'_c = a' \quad \text{and} \quad y'_c = b' \tag{36}$$

If $-\frac{L}{2} < x'_c < \frac{L}{2}$ and $H < y'_c < H + W$, it means that the center of the circle is in fault area and main part of the circle lies on fault range, otherwise there is only small part of the circle lies on fault.

Depends on the position of intersection circle's center, there are two main approach to calculate the area between intersection curves.

1. If intersection circle's center is in fault range ($-\frac{L}{2} < x'_c < \frac{L}{2}$ and $H < y'_c < H+W$).

I. In the first case, there are two intersections between the circle and each rectangle's edge.

$$A_i = \left(\pi - \sum_{j=1}^{J} \frac{\left(\alpha_j - \sin\alpha_j\right)}{2} \right) * \bar{R}_i^{\,2} \tag{37}$$

where A_i is the area of intersection between fault plane and hypothetical sphere, J is number of circle's parts lie out of fault and $\bar{R}_i$ is the radius of intersection circle. $\bar{R}_i$ and α_j may be written as:

$$\bar{R}_i = \sqrt{r_i^2 - D_i^2} \tag{38}$$

where D_i is the shortest distance between the center of sphere (position of site) and fault plane, whose equation is $a_1 x' + b_1 y' + c_1 z' + d = 0$.

$$D_i = \frac{\left| a_1 a' + b_1 b' + c_1 c' + d \right|}{\sqrt{a_1^2 + b_1^2 + c_1^2}} \tag{39}$$

And finally,

$$\alpha_j = \pi - \cos^{-1} \frac{k}{2\bar{R}_i} \tag{40}$$

where based on the position of outside parts of circle, (up, side or down edge) k could be:

$$k = 2 * \sqrt{r_1^2 - c'^2 - \left(H - b'\right)^2} \quad \text{for up edge} \tag{41}$$

$$k = 2 * \sqrt{r_1^2 - c'^2 - \left(\pm\frac{L}{2} - a'\right)^2} \quad \text{for side edge} \tag{42}$$

$$k = 2 * \sqrt{r_1^2 - c'^2 - \left(H + W - b'\right)^2} \quad \text{for down edge} \tag{43}$$

II. In the second case, there is one intersection between the circle and each rectangle's edge (for example, there are two intersections on top and right edge of rectangle).

$$A_i = \frac{\left(\alpha - \sin\alpha\right) * \bar{R}_i^{\,2}}{2} - Q \tag{44}$$

which α and Q come from Equations (45) and (46).

$$\alpha = \pi - \cos^{-1} \frac{2 * \sqrt{r_i^2 - c'^2 - \left(\frac{L}{2} + a'\right)^2}}{2\bar{R}_i} \tag{45}$$

$$Q = \left[\left(H - b'\right)\left(a' + L/2\right) + \Gamma_2/8 \left(2a' + L\right) \times \frac{1}{2}\left(r_i^2 - c'^2\right)\left(tan^{-1}\left(\frac{\left(L + 2a'\right)}{\Gamma_2} \right)\right) + \left(H - b'\right)\left[\Gamma_3 + \frac{1}{2}\Gamma_3 \, sgn\left(H - b'\right) \right] \right] \tag{46}$$

2. If intersection circle's center is not in fault range ($-\frac{L}{2} \geq x'_c$, $x'_c \geq \frac{L}{2}$, $H \geq y'_c$ or $y'_c \geq H + W$). The area between the first top curve and the top boundary of the rectangular fault plane may be easily calculated by integral in Equation (47).

$$A_i = \int_{Ll}^{Rl} \int_{Bl}^{Tl} d\,y\,d\,x \tag{47}$$

in which *Ll*, *Rl*, *Bl*, and *Tl* denote the left, right, bottom, and top limits of the integral. Based on integral limits, A_i would be:

I. In the first case: $Ll = -\frac{L}{2}$, $Rl = \frac{L}{2}$, $Dl = H$, $Ul = \sqrt{r_1^2 - c'^2 - \left(x' - a'\right)^2} + b'$, and,

$$A_i = b'L - HL + \frac{1}{8}\Gamma_1\left(L - 2a'\right) + \frac{1}{2}\left(r_i^2 - c'^2\right) \times \left(tan^{-1}\left(\frac{\left(L - 2a'\right)\left(\Gamma_1 + \Gamma_2\right)}{\Gamma_1\Gamma_2 - \left(L - 2a'\right)^2} \right) + \kappa_1\pi \right) + \frac{1}{8}\Gamma_2\left(L + 2a'\right) \tag{48}$$

where $\kappa_1 = 0$ for $\frac{\left(L - 2a'\right)^2}{\Gamma_1\Gamma_2} < 1$, and otherwise $\kappa_1 = 1$.

II. In the second case: $Ll = -\frac{L}{2}$, $Rl = \sqrt{r_1^2 - c'^2 - \left(H - b'\right)^2} + a'$, $Dl = H$, $Ul = \sqrt{r_1^2 - c'^2 - \left(x' - a'\right)^2} + b'$, and,

$$A_i = \left(b' - H\right) * \left(a' + \frac{1}{2}L \right) + \frac{1}{2}\Gamma_3 \times \left[sgn\left(H - b'\right)H - sgn\left(H - b'\right)b' + 2b' - 2H \right] + \frac{1}{2}\left(r_i^2 - c'^2\right)\left(tan^{-1} \times \left(\frac{\Gamma_2\Gamma_3 sgn\left(H - b'\right) + \left(H - b'\right)\left(L + 2a'\right)}{\Gamma_2\left(H - b'\right) - \Gamma_3\left(L + 2a'\right) sgn\left(H - b'\right)} \right) + \kappa_2\pi \right) + \frac{1}{8}\Gamma_2\left(L + 2a'\right) \tag{49}$$

where $\kappa_2 = 0$ for $\frac{\Gamma_3(L+2a)\,sgn(H-b)}{\Gamma_2(H-b)} < 1$, and otherwise $\kappa_2 = 1$.

III. In the third case:

$$l = -\sqrt{r_1^2 - c'^2 - (H-b')^2} + a',$$

$$Rl = \frac{L}{2},\ Dl = H,$$

$$Ul = \sqrt{r_1^2 - c'^2 - (x'-a')^2} + b',$$

and

$$A_i = (b'-H)\left(a' + \frac{1}{2}L\right) + \frac{1}{8}\Gamma_1(L-2a') + \frac{1}{2}(r_i^2 - c'^2)\times\left(tan^{-1}\times\left(\frac{\Gamma_1\Gamma_3 sgn(H-b') + (H-b')(L+2a')}{\Gamma_1(H-b') - \Gamma_3(L+2a')\,sgn(H-b')}\right) + \kappa_3\pi\right) + \frac{1}{2}\Gamma_3\left[sgn(H-b')H - sgn(H-b')\,b' + 2b' - 2H\right] \quad (50)$$

where $\kappa_3 = 0$ for $\frac{\Gamma_3(L+2a')\,sgn(H-b')}{\Gamma_1(H-b')} < 1$, and otherwise $\kappa_3 = 1$.

$$\Gamma_1 = \sqrt{-L^2 + 4La' - 4a'^2 - 4c'^2 + 4r_i^2} \quad (51)$$

$$\Gamma_2 = \sqrt{-L^2 - 4La' - 4a'^2 - 4c'^2 + 4r_i^2} \quad (52)$$

$$\Gamma_3 = \sqrt{-H^2 + 2Hb' - b'^2 - c'^2 + r_i^2} \quad (53)$$

when there are intersections between the curve and lower boundary, for which the integral should be divided into different parts with different limits.

The area between other curves may come from the following relation:

$$A_{s_i} = A_i - \sum_{j=1}^{i-1} A_{s_j};\quad i = 2, 3, 4, \ldots \quad (54)$$

while for $i = 1$, $A_{s_1} = A_1$

The above conditions are computed, whose final results are summarized as given in the following ones:

As already mentioned, A_{s_i} denotes the area of zone between two adjacent $(i)^{th}$ and $(i+1)^{th}$ curves on the fault, and the arrival time of seismic waves came from this part would be

$$t_{s_i} = \frac{1}{V_S}\left(R_{s_i} - R_{min}\right) \quad (55)$$

where R_{s_i} indicates the radius of $(i)^{th}$ sphere, R_{min} denotes the shortest distance between the receiver and the fault (see Figure 4), and V_S is the velocity of S wave.

To calculate the second part of arrival time of seismic waves, regarding of position of hypocenter, areas between two adjacent curves must themselves divide to portions with different distance from hypocenter. In order to specify the areas with the same distance from the hypocenter on each A_{s_i}, several circles of various radius are drawn whose centers are located on the given hypocenter. All points in the region between the parallel curves are considered to have the same distance from the hypocenter which means that all points surrounded by two adjacent $(j)^{th}$ and $(j+1)^{th}$ curves would rupture together. The arrival time of the rupture for this part would be:

$$t_{h_j} = \frac{1}{V_r}\left(R_{h_j}\right) \quad (56)$$

where R_{h_j} indicates distance between the hypocenter and $(j)^{th}$ part of the fault and V_r is the velocity of the rupture. The probability of that S waves get to the receiver, in $t_{sh_{ij}}$, may be given by:

$$P_A(a_{i,j}) = \frac{A_{sh_{ij}}}{A} \quad (57)$$

where $A_{sh_{ij}}$ is the area of portion surrounded by adjacent $(j)^{th}$, $(j+1)^{th}$, $(i)^{th}$, $(i+1)^{th}$ curves (see Figure 5) also A is the whole area of the fault. In addition,

$$t_{sh_{ij}} = t_{s_i} + t_{h_j} \quad (58)$$

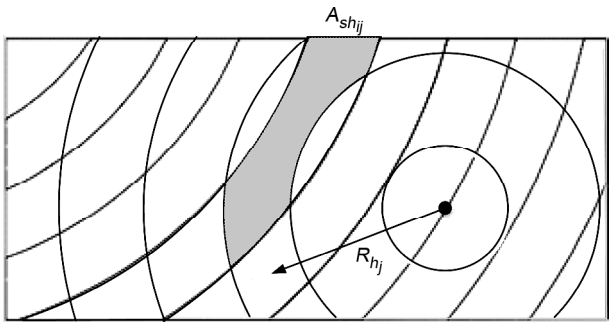

Figure 5. $A_{sh_{ij}}$ is area of portion surrounded by adjacent $(j)^{th}$ and $(j+1)^{th}$ curves, which are related to position of hypocenter and $(i)^{th}$ and $(i+1)^{th}$ curves, which are related to site position.

Figure (6) shows division of fault plane based on the distance from the receiver location and also the position of hypocenter in the middle of fault. Besides, Figure (7) shows the procedure of preparing PDF of arrival time. Figure (8) to Figure (10) illustrate the time functions obtained from the mentioned PDF for each receiver position with the same distances from the fault but in different directions, respectively.

5. Results and Discussion

In this study, a rectangular fault with dimensions of 20 x 10 km^2 located in 15 km depth and three

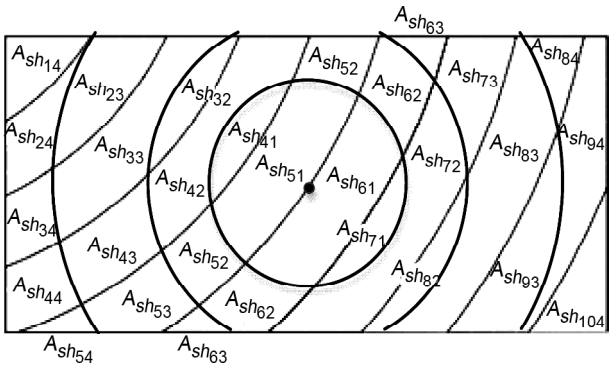

Figure 6. Fault plane divided based on the distance from the receiver position by curves produced by intersecting the fault plane with the spheres whose centers are located on the receiver positions No. 1 indicated in Figure (2) and considering a hypocenter in the center of fault plane.

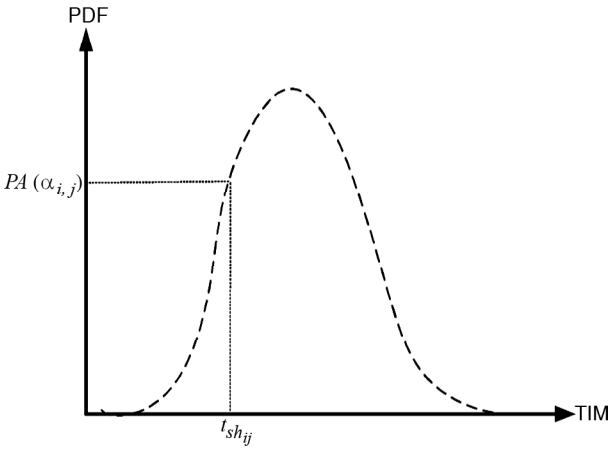

Figure 7. The PDF of arrival times for the considered hypocenter and site position.

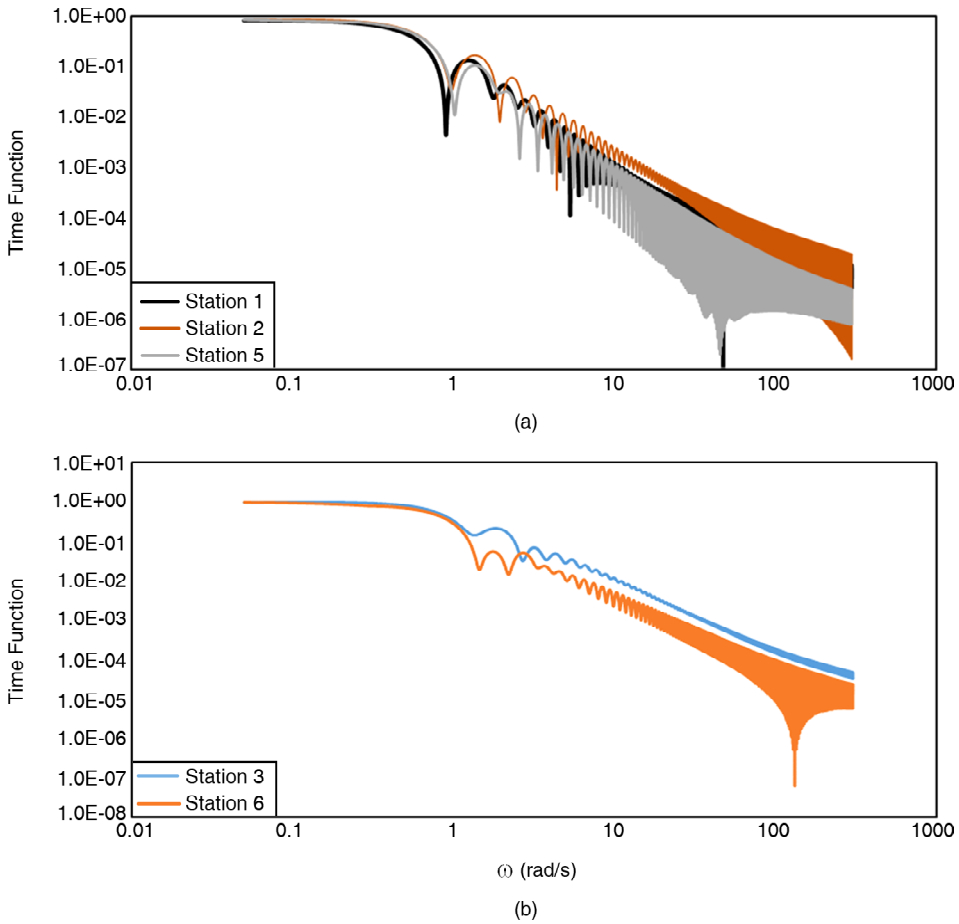

Figure 8. Expected values of time functions for source spectra derived by the new PDFs of arrival time, produced by intersecting the fault plane with the spheres whose centers are located on the receiver positions of (a) No. 1, 2 and 5, (b) No. 3 and 6, (c) No. 4 and 7. Mentioned stations on each diagram have the same position related to the fault but on different side of it. The mentioned numbers are indicated in Figure (2). α for all diagrams is 20.

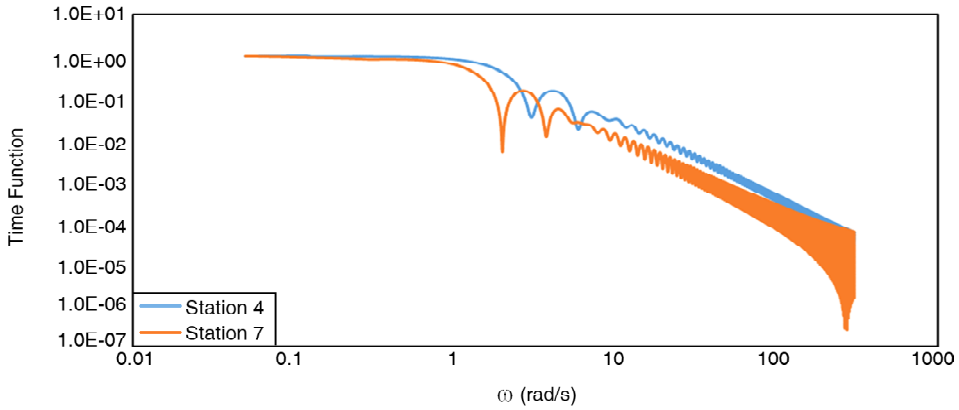

(c)

Figure 8. Continue.

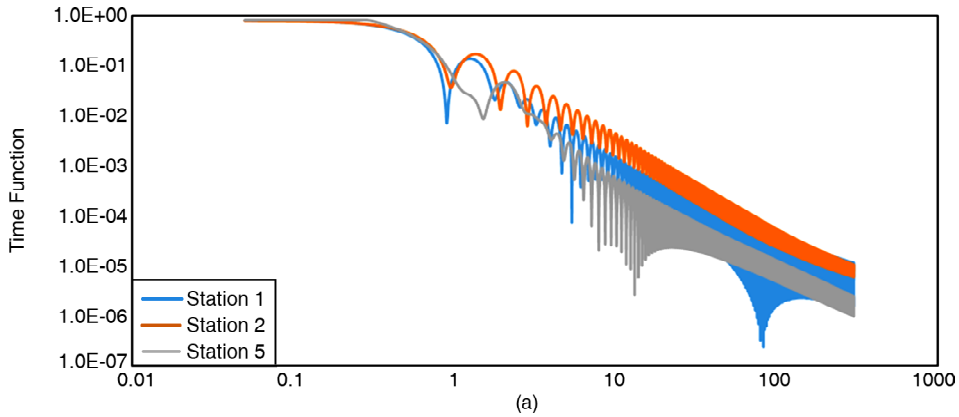

(a)

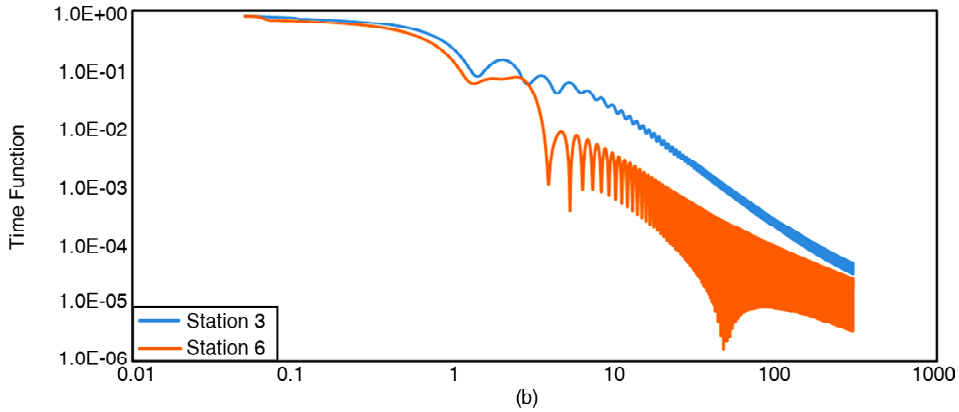

(b)

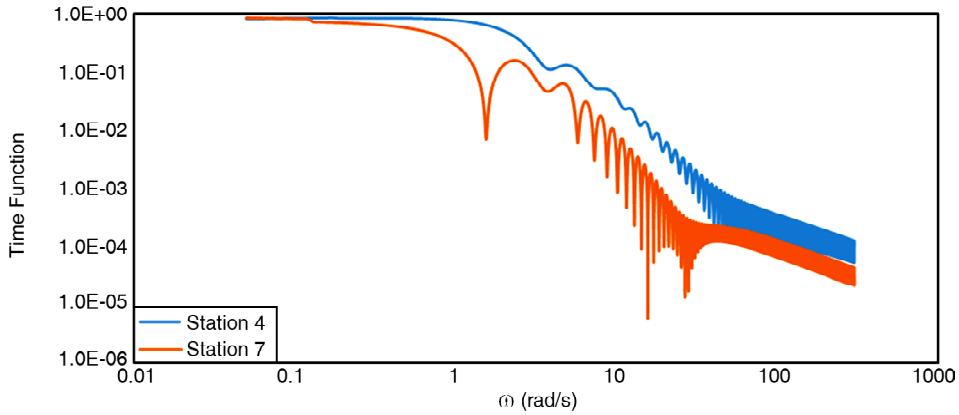

(c)

Figure 9. Expected values of time functions for source spectra derived by the new PDFs of arrival time, produced by intersecting the fault plane with the spheres whose centers are located on the receiver positions of (a) No. 1, 2 and 5, (b) No. 3 and 6, (c) No. 4 and 7. Mentioned stations on each diagram have the same position related to the fault but on different side of it. The mentioned numbers are indicated in Figure (2). α for all diagrams is 40.

different rotate angles, is considered ($\alpha = 20$, 40 and 60°). The receiver positions are assumed in 60 km distances and seven different directions from the fault. Figure (2) illustrates the position of selected sites and the geometry of fault. As mentioned before, to specify the first part of total time, fault surface divided to different areas with specific distance from the receiver. To do so, different spheres have been drawn that their center lie on position of stations. Figure (4) shows curves and sections on the fault caused by intersecting spheres and the fault plane (see Equations (29 to 54) for more details). To calculate the second part, each section should be divided to its own subsections based on the distance from the hypo-center, as shown in Figure (5) (see Equations 55 and 56). By this approach, all points of the fault are categorized based on their distance from

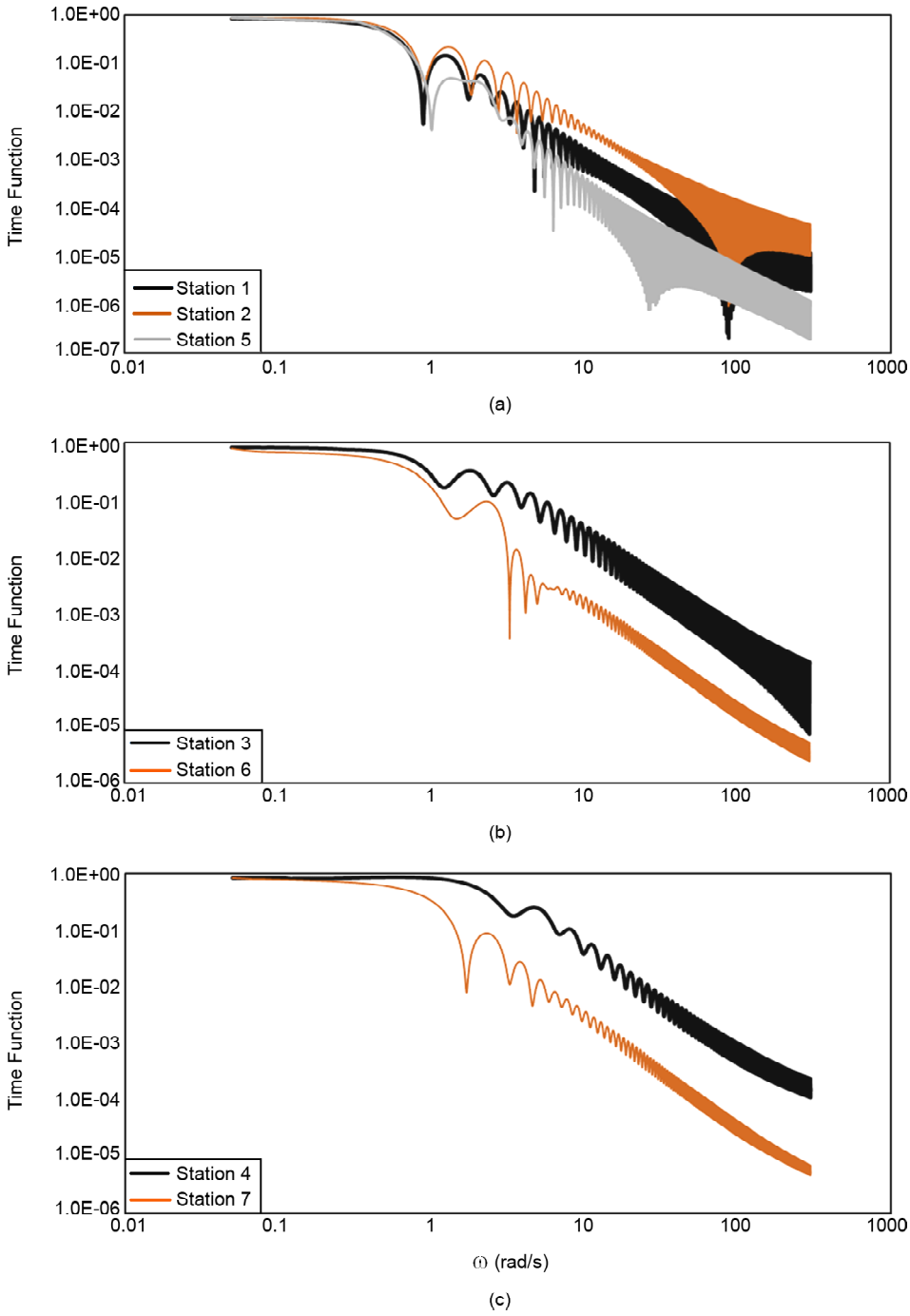

Figure 10. Expected values of time functions for source spectra derived by the new PDFs of arrival time, produced by intersecting the fault plane with the spheres whose centers are located on the receiver positions of (a) No. 1, 2 and 5, (b) No. 3 and 6, (c) No. 4 and 7. Mentioned stations on each diagram have the same position related to the fault but on different side of it. The mentioned numbers are indicated in Figure (2). α for all diagrams is 60.

hypocenter as well as site position (namely, total time of arrival may be calculated). By dividing the area of each subsection by total area, the probability of arriving seismic waves caused by subsection in defined time window, is obtained (see Figure 7).

To illustrate the effect of inclined fault on time functions of stations with the same distance from the fault but on different side of the fault, Figure (8) shows time functions belong to stations on both sides of the fault for $\alpha = 20$. Besides, Figures (9) and (10) show the same functions for $\alpha = 40$ and 60 respectively. As already mentioned, to calculate these time functions, non-uniform PDFs of arrival waves described in previous section, is used in Equation (10). As may be observed from Figures (8) to (10), decreasing effects of time functions on the source spectra in stations on left side of the fault (stations 2, 3 and 4) is less than those on right side of the fault (stations 5, 6 and 7). Besides, from Figures (8) to (10), it is observable that the difference between time functions belong to stations on both sides of the fault, increases by increasing amount of α. In other word, the difference between time functions of left and righthand stations when $\alpha = 20$ is less than when $\alpha = 60$.

Figure (11) shows time functions for the same station but different rotation of fault plane. As it shows in Figure (11), in stations on left hand side of the fault, by increasing rotation (increasing amount of α) decreasing effects of time functions are reduced. It means that the time function of each station when $\alpha = 60$ has higher level than when $\alpha = 20$. However, on right hand side of the fault results are opposite of left hand side. From Figure (11), it is observable that on right hand side of the fault (stations 5, 6 and 7), by increasing rotation (increasing amount of α) decreasing effects of time functions increase.

Using new time functions for inclined fault introduced in this study, Figure (12) represents earthquake source acceleration spectra of the SBM for inclined fault with rotation angle of 20

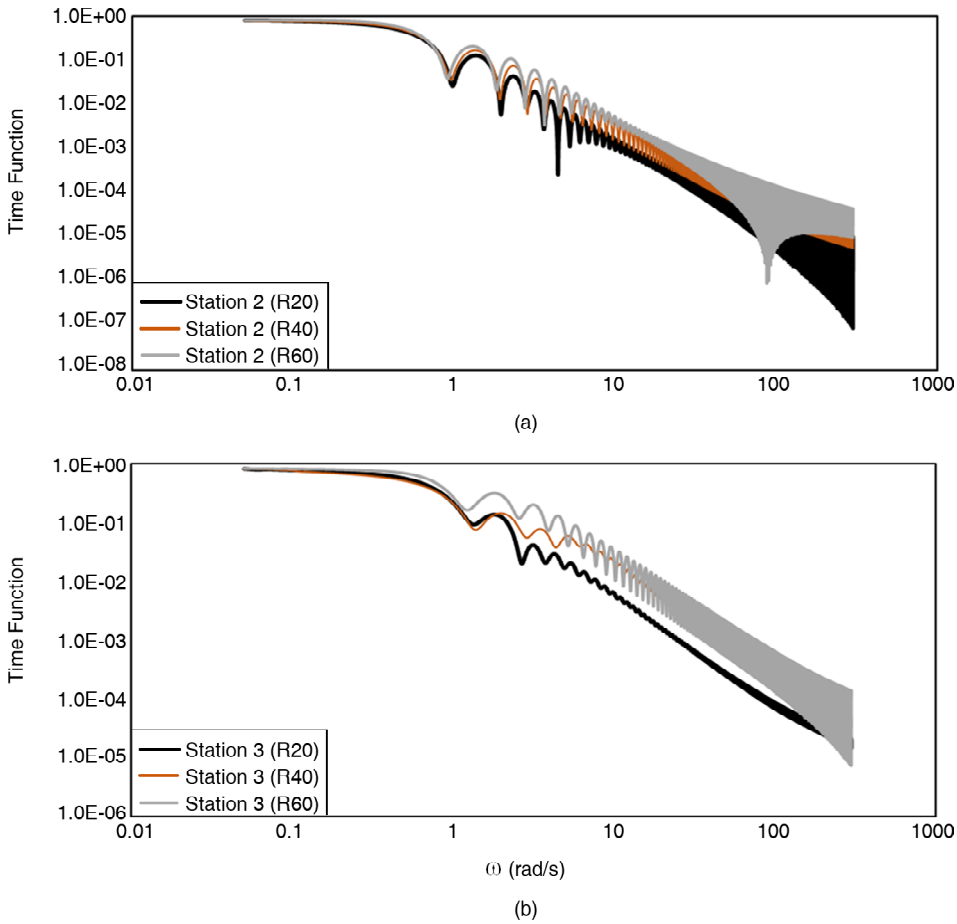

Figure 11. Expected values of time functions for source spectra with three different rotation angle of fault plane (α =20,40 and 60) for receiver positions of (a) No. 2, (b) No. 3, (c) No. 4, (d) No.5, (e) No. 6 and (f) No.7. Mentioned stations on each diagram have the same position related to the fault but on different side of it. The mentioned numbers are indicated in Figure (2).

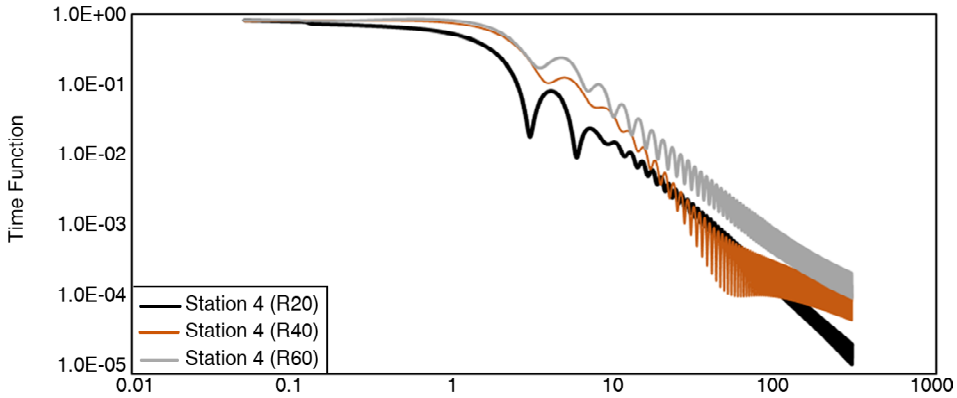

(c)

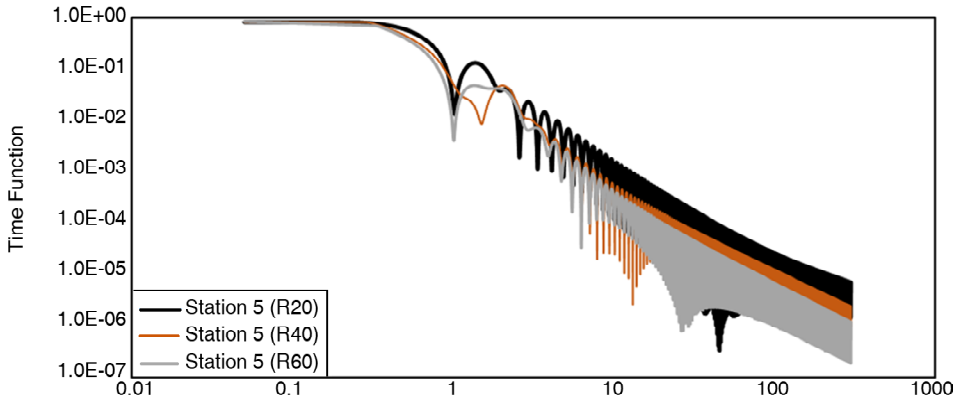

(d)

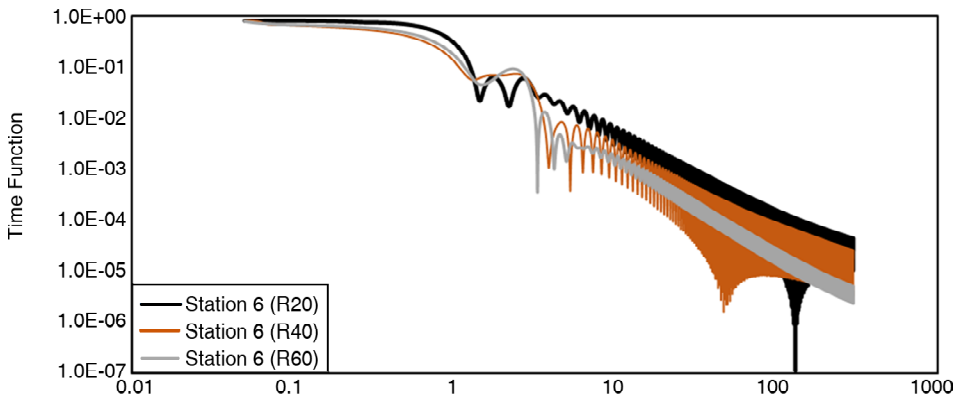

(e)

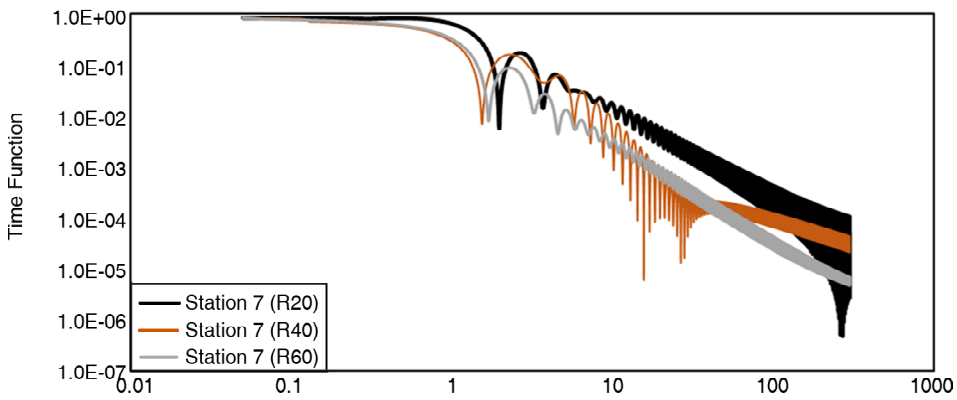

(f)

Figure 11. Continue.

(α = 20) and with fractal distributions of subevent sizes, for which fractal dimensions are 2 and 3, respectively. This figure obviously shows the effect of site position (relative to the fault) on source spectra of earthquake. As already mentioned, shorter duration of receiving energy causes increasing spectra level in intermediate frequencies. Figure (12) shows that the stations across the fault with shorter duration of receiving energy have higher spectra level at intermediate frequencies. Besides, it is observable that stations on left hand side have higher spectra level at intermediate frequencies for the same reason. Thus, station no. 4 has highest spectra level at intermediate frequencies among others. Figures (13) and (14) show the same earthquake source acceleration spectra of the SBM for inclined fault but for different rotation angles (α = 40 and 60 respectively) as well as the same fractal

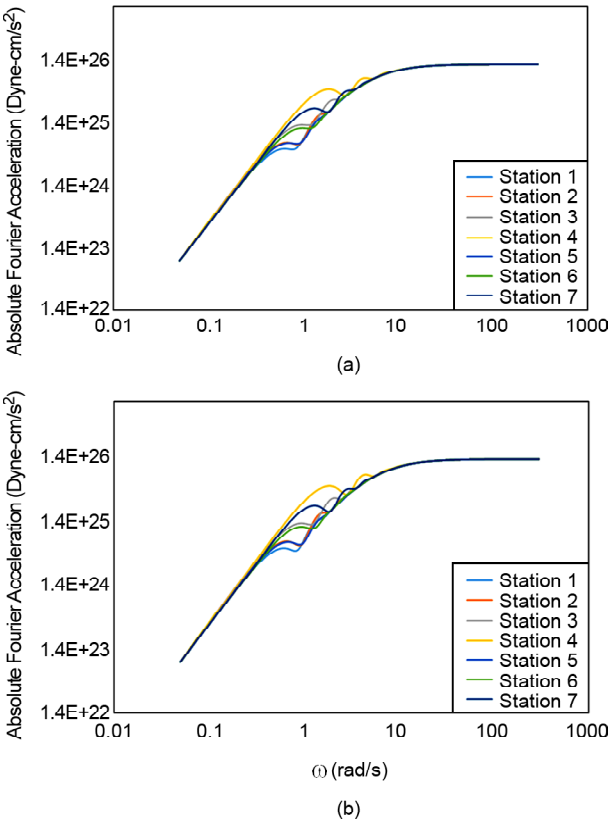

Figure 12. Earthquake source acceleration spectra for the SBM with fractal distributions of subevent sizes, for which D is assumed (a) 2, (b) 3. The mentioned numbers are indicated in Figure (2). α for all diagrams is 20.

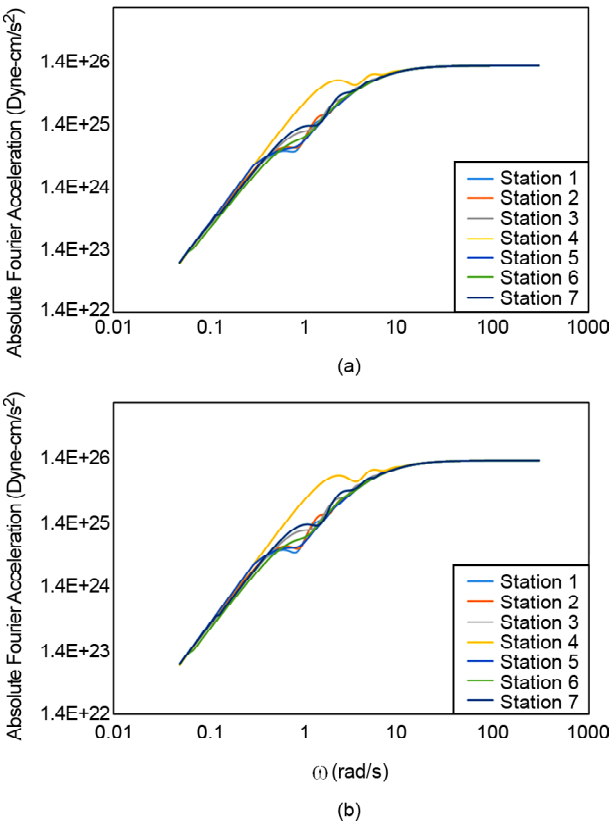

Figure 13. Earthquake source acceleration spectra for the SBM with fractal distributions of subevent sizes, for which D is assumed (a) 2, (b) 3. The mentioned numbers are indicated in Figure (2). α for all diagrams is 40.

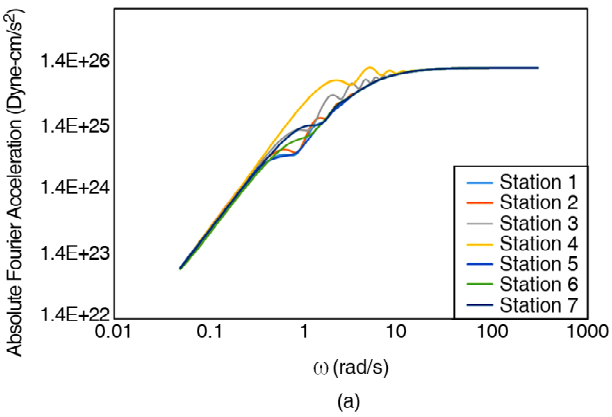

Figure 14. Earthquake source acceleration spectra for the SBM with fractal distributions of subevent sizes, for which D is assumed (a) 2, (b) 3. The mentioned numbers are indicated in Figure (2). α for all diagrams is 60.

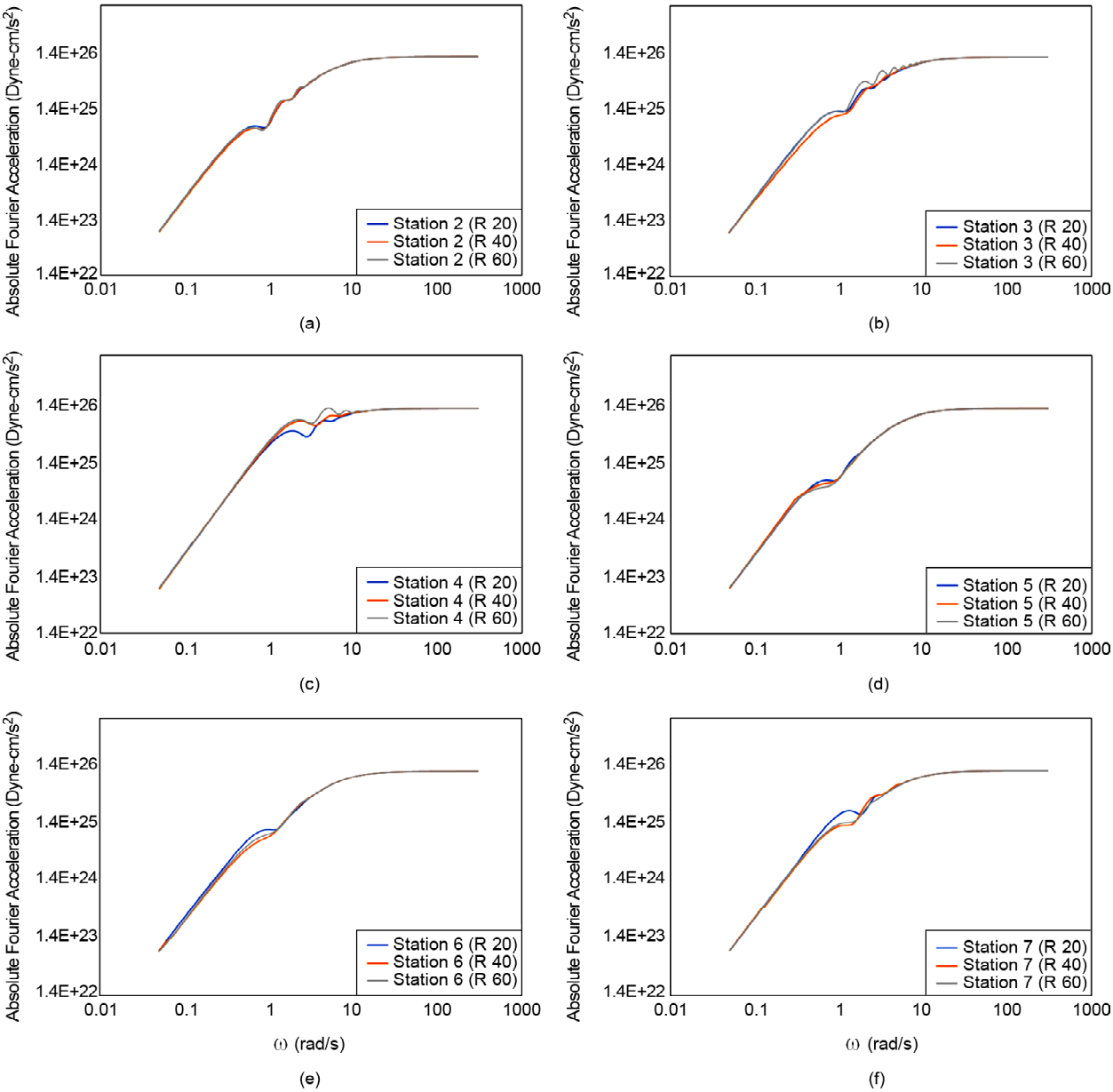

Figure 15. Earthquake source acceleration spectra for the SBM with fractal distributions of subevent sizes, for which D is assumed 2, using new time function derived by the new PDFs of arrival time for three different rotation angles of fault plane (α = 20, 40 and 60) for receiver positions of (a) No. 2, (b) No. 3, (c) No. 4, (d) No.5, (e) No. 6 and (f) No.7. Mentioned stations on each diagram have the same position related to the fault but on different side of it. The mentioned numbers are indicated in Figure (2).

distributions of subevent sizes.

To demonstrate the effect of fault rotation on source spectra, Figures (15) and (16) showing earthquake source acceleration spectra of the SBM for each station with three different rotation angles (α = 20, 40 and 60) with fractal distributions of subevent sizes, for which fractal dimensions are 2 and 3, respectively. As expected in station across the fault, difference between source spectra (especially in intermediate frequencies) is much more than stations along the fault. In the station on left hand side, amount of source spectra, increases by increasing rotation of fault plane (increasing amount of α) but on the other side (right hand side), the results are inverse.

6. Conclusions

The SBM, as a simple and realistic composite source model, simulates seismic ground motions using the stochastic modeling approach. The far-field spectrum obtained by the mentioned earthquake source model may be affected by statistical characteristics of the subevents and arrival time of seismic waves. Characteristics of the subevents (i.e., the number and size of subevents) may cause differences in high-frequency zone of the spectra;

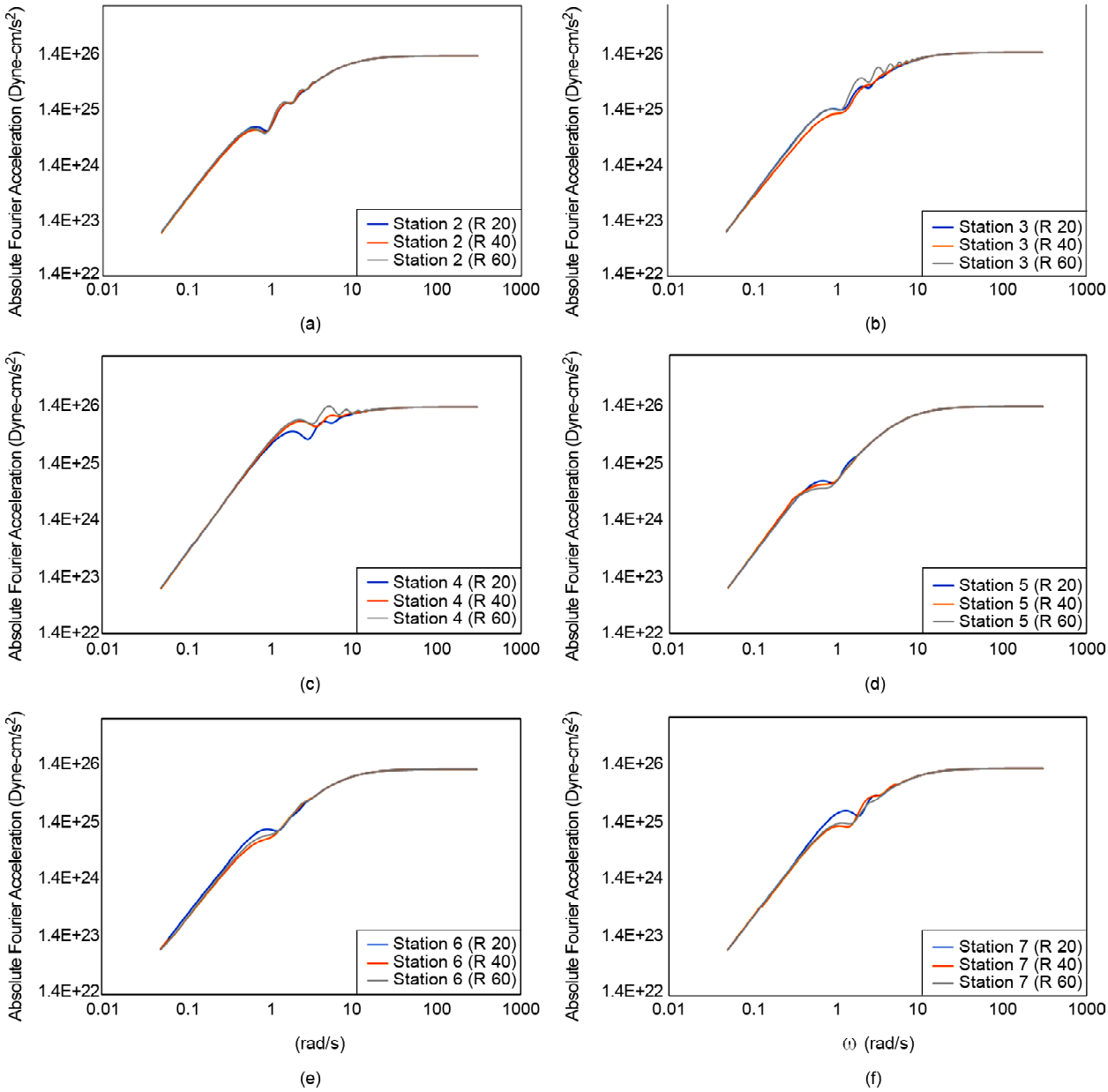

Figure 16. Earthquake source acceleration spectra for the SBM with fractal distributions of subevent sizes, for which D is assumed 3, using new time function derived by the new PDFs of arrival time for three different rotation angle of fault plane (α = 20, 40 and 60) for receiver positions of (a) No. 2, (b) No. 3, (c) No. 4, (d) No. 5, (e) No. 6 and (f) No. 7. Mentioned stations on each diagram have the same position related to the fault but on different side of it. The mentioned numbers are indicated in Figure (2).

however, middle-frequency zone of the spectra may be influenced by the shape of time functions. To examine the effect of fault geometry, receiver's position and also the rotation of fault plane on the source spectra, modified time functions based on new PDF of arrival times has been proposed in this study. By choosing receiver positions in four different directions on both sides of the fault (seven different site positions) and three rotation angles for fault plane, the effects of site position, fault geometry and rotation of fault plane on obtained time functions as well as the source spectra have been illustrated. Based on the obtained results, decreasing effects of time functions on the source spectra in points across the fault is less than those along the fault. Therefore, general stations along the fault have lower spectral levels at intermediate frequencies, compared to those across the fault. Moreover, decreasing effects of time functions on the source spectra in stations on left side of the fault (stations 2, 3 and 4) is less than those on right side of the fault (stations 5, 6 and 7). In other words, because of its position on left hand side and across the fault, station 4 has highest spectral levels at

intermediate frequencies among other stations. Besides, it is obvious that the difference between time functions belong to stations on the same position related to the fault but on different side of the fault, increases by increasing amount of rotation. This fact is attributed to the shape of PDF as well as the duration of arriving seismic energy.

References

1. Papageorgiou, A.S. and Aki, K. (1983a) A specific barrier model for the quantitative description of inhomogeneous faulting and the prediction of strong ground motion. I. Description of the model. *Bulletin of Seismological Society of America*, **73**(3), 693-722.

2. Papageorgiou, A.S. and Aki, K. (1983b) A specific barrier model for the quantitative description of inhomogeneous faulting and the prediction of strong ground motion. Part II. Applications of the model. *Bulletin of Seismological Society of America*, **73**(4), 953-978.

3. Aki, K. (1967) Scaling law of seismic spectrum. *Journal of Geophysical Research*, **72**(4), 1217-1231.

4. Brune, J.N. (1970) Tectonic stress and the spectra of seismic shear waves from earthquakes. *Journal of Geophysical Research*, **75**(26), 4997-5009.

5. Boore, D.M. (2003) Prediction of ground motion using stochastic method. *Pure and Applied Geophysics*, **160**(12), 635-676.

6. Halldorsson, B. and Papageorgiou, A.S. (2005) Calibration of the specific barrier model to earthquakes of different tectonic regions. *Bulletin of Seismological Society of America*, **95**(4), 1276-1300.

7. Zafarani, H., Mousavi, M., Noorzad, A., and Ansari, A. (2008) Calibration of the specific barrier model to Iranian plateau earthquakes and development of physically based attenuation relationships for Iran. *Soil Dynamics and Earthquake Engineering*, **28**(7), 550-576.

8. Soghrat, M.R., Khaji, N., and Zafarani, H. (2012) Simulation of strong ground motion in northern Iran using the specific barrier model. *Geophysical Journal International*, **188**(2), 645-679.

9. Mousavi, M., Zafarani, H., Noorzad, A., Ansari, A., and Bargi, K. (2007) Analysis of Iranian strong-motion data using the specific barrier model. *Journal of Geophysical Engineering*, **4**(4), 415-428.

10. Papageorgiou, A.S. (2003) The barrier model and strong ground motion. *Pure and Applied Geophysics*, **160** (3-4), 603-634.

11. Frankel, A. (1991) High-frequency spectral falloff of earthquakes, fractal dimension of complex rupture, b value, and the scaling of strength on faults. *Journal of Geophysical Research*, **96**(2), 6291-6302.

12. Zeng, Y, Anderson, J.G., and Yu, G. (1994) A composite source model for computing realistic synthetic strong ground motions. *Geophysical Research Letters*, **21**, 725-728.

13. Halldorsson, B. and Papageorgiou, A.S. (2012) Variations of the specific barrier model-part I: effect of subevent size distributions. *Bulletin of Earthquake Engineering*, **10**(4), 1299-1319.

14. Halldorsson, B. and Papageorgiou, A.S. (2012) Variations of the specific barrier model-part II: effect of isochron distributions. *Bulletin of Earthquake Engineering*, **10**(4), 1321-1337.

15. Papageorgiou, A.S. and Aki, K. (1985) Scaling law of far-field spectra based on observed parameters of the specific barrier model. *Pure and Applied Geophysics*, **123**(2), 353-374.

16. Papageorgiou, A.S. (1988) On two characteristic frequencies of acceleration spectra: patch corner frequency and fmax. *Bulletin of Seismological Society of America*, **78**(2), 509-529.